MATERIALS SCIENCE

Retarding solid-state reactions enable efficient and stable all-inorganic perovskite solar cells and modules

Cheng Liu[1,2]†, Xiuhong Sun[3]†, Yi Yang[1,2]†, Olga A. Syzgantseva[4], Maria A. Syzgantseva[4,5], Bin Ding[2], Naoyuki Shibayama[6], Hiroyuki Kanda[2], Farzaneh Fadaei Tirani[2], Rosario Scopelliti[2], Shunlin Zhang[7], Keith G. Brooks[2], Songyuan Dai[1], Guanglei Cui[3], Michael D. Irwin[8], Zhipeng Shao[3]*, Yong Ding[1,2]*, Zhaofu Fei[2]*, Paul J. Dyson[2]*, Mohammad Khaja Nazeeruddin[2,9]*

All-inorganic $CsPbI_3$ perovskite solar cells (PSCs) with efficiencies exceeding 20% are ideal candidates for application in large-scale tandem solar cells. However, there are still two major obstacles hindering their scale-up: (i) the inhomogeneous solid-state synthesis process and (ii) the inferior stability of the photoactive $CsPbI_3$ black phase. Here, we have used a thermally stable ionic liquid, *bis*(triphenylphosphine)iminium *bis*(trifluoromethylsulfonyl)imide ([PPN][TFSI]), to retard the high-temperature solid-state reaction between Cs_4PbI_6 and $DMAPbI_3$ [dimethylammonium (DMA)], which enables the preparation of high-quality and large-area $CsPbI_3$ films in the air. Because of the strong Pb-O contacts, [PPN][TFSI] increases the formation energy of superficial vacancies and prevents the undesired phase degradation of $CsPbI_3$. The resulting PSCs attained a power conversion efficiency (PCE) of 20.64% (certified 19.69%) with long-term operational stability over 1000 hours. A record efficiency of 16.89% for an all-inorganic perovskite solar module was achieved, with an active area of 28.17 cm^2.

INTRODUCTION

All-inorganic perovskites without volatile components have been considered as promising photovoltaic (PV) materials with which to solve the thermal instability issues faced by perovskite solar cells (PSCs) and thereby move them toward real-world applications (*1–5*). Among these perovskites, black-phase $CsPbI_3$ has the most appropriate bandgap (E_g) of ~1.70 eV to serve as the light harvester in a solar cell and is particularly suited to the top cell of a tandem solar cell (*6, 7*). Over the past few years, $CsPbI_3$ PSCs have undergone rapid development (*8, 9*). However, the thermodynamically preferred crystal structure of $CsPbI_3$ is the nonphotoactive yellow phase (δ) with E_g of 2.82 eV at room temperature (RT) due to its imperfect Goldschmidt tolerance factor (*10, 11*). These problems reduce the uptake of $CsPbI_3$ PSCs by the PV community.

To enhance the PV performance and stability of $CsPbI_3$ PSCs, several strategies have been developed, including interface modification (*12–16*), ion substitution (*17–20*), crystallization regulation (*21–23*), and others (*24, 25*). A milestone in the improvement of the efficiencies of these PSCs was the incorporation of dimethylammonium iodide (DMAI) to form the $DMAPbI_3$ intermediate, which

stabilizes the black phase of $CsPbI_3$ at RT and opens up the possibility of its scale-up in the ambient air (*26, 27*). It was also found that changing the annealing atmosphere from an inert gas to air can not only accelerate the evaporation of residual DMAI but also accelerate the ion exchange and phase transition (fig. S1) (*28*). This could affect the device performance and the reproducibility due to the generation of abundant defects during the inhomogeneous high-temperature (>180°C) solid-state reaction in the $CsPbI_3$ films (*29–32*). Therefore, an effective method is sought to prepare stable and low-defect $CsPbI_3$ films under ambient conditions. This is imperative to the development of all-inorganic PSCs and their possible future large-scale application (*33–37*).

Ionic liquids (ILs) with high thermal stability have been applied in PSCs, resulting in improved device stability and performance (*38, 39*). Unlike commonly applied ILs containing [PF_6] and [BF_4] anions, ILs with [TFSI] [*bis*(trifluoromethylsulfonyl)imide] anion is highly coordinating, its O or N in the anion being able to act as both monodentate and bidentate ligands to form dative bonds to almost all metals (*40, 41*). By applying salts with bulky, highly hydrophobic *bis*(triphenylphosphine)iminium ([PPN]) groups in the cation, together with presence of the hydrophobic CF_3 groups in the anion, the overall stability against moisture should be boosted.

Here, we describe the incorporation of a thermally stable IL, [PPN][TFSI], into the $CsPbI_3$ absorber to afford high-performance all-inorganic PSCs and modules. The experimental and theoretical results support the conclusion that [PPN][TFSI] (i) interacts with the $DMAPbI_3$ intermediate to slow down the ion exchange and solid-state reaction, thereby increasing the $CsPbI_3$ grain size to the micrometer scale; (ii) increases the energy of superficial vacancy formation and reduces the defect densities; and (iii) forms strong interactions with $CsPbI_3$ to prevent its phase transition to the undesired δ phase. We report a power conversion efficiency (PCE) of 20.64% (certified 19.69%) for $CsPbI_3$ PSCs where the IL has been included, which also shows long-term operational stability (88% PCE retention after 1000 hours). The ensuing all-inorganic

[1]State Key Laboratory of Alternate Electrical Power System with Renewable Energy Sources, North China Electric Power University, Beijing 102206, China. [2]Institute of Chemical Sciences and Engineering, École Polytechnique Fédérale de Lausanne (EPFL), CH-1015 Lausanne, Switzerland. [3]Qingdao Institute of Bioenergy and Bioprocess Technology, Chinese Academy of Sciences, Qingdao 266101, China. [4]Department of Chemistry, Lomonosov Moscow State University, Moscow 119991, Russia. [5]Department of Nanotechnology and Nanomaterials, Mendeleev University of Chemical Technology, Moscow 125047, Russia. [6]Department of Clinical Engineering, Toin Yokohama University, 1614 Kurogane, Aoba, Yokohama, Japan. [7]College of Chemistry and Chemical Engineering, Guizhou University, Guiyang 550025, China. [8]CubicPV Inc., 1807 Ross Ave, Ste 333, Dallas, TX 75201, USA. [9]Department of Materials Science and Engineering, City University of Hong Kong, Kowloon, Hong Kong, China.
*Corresponding author. Email: shaozp@qibebt.ac.cn (Z.S.); dingy@ncepu.edu.cn (Y.D.); zhaofu.fei@epfl.ch (Z.F.); paul.dyson@epfl.ch (P.J.D.); mdkhaja.nazeeruddin@epfl.ch (M.K.N.)
†These authors contributed equally to this work.

perovskite solar module with an active area of 28.17 cm^2 represents a record efficiency of 16.89%.

RESULTS

The effect of [PPN][TFSI] on the solid-state reaction

A typical DMAI-assisted CsPbI$_3$ formation process includes four steps: (i) self-assembly of the DMAPbI$_3$-Cs$_4$PbI$_6$-mixed film by spin coating a precursor solution containing CsI, PbI$_2$, and DMAI; (ii) the solid-state reaction between DMAPbI$_3$ and Cs$_4$PbI$_6$ to form DMA-doped CsPbI$_3$ perovskite γ-DMA$_x$Cs$_{1-x}$PbI$_3$; (iii) further reaction of γ-DMA$_x$Cs$_{1-x}$PbI$_3$ with Cs$_4$PbI$_6$ into undoped γ-CsPbI$_3$; and (iv) the undesired phase transformation of γ-CsPbI$_3$ into its nonperovskite yellow phase δ-CsPbI$_3$. When upscaling is desired, a large scale inhomogeneous solid-state reaction such as this is a hindrance due to the coexistence of DMAPbI$_3$, Cs$_4$PbI$_6$, γ-DMA$_x$Cs$_{1-x}$PbI$_3$, γ-CsPbI$_3$, and δ-CsPbI$_3$, which will lead to high defect densities and subsequent lowering of PCE (28–37, 42).

In this work, we investigated the [PPN][TFSI] IL toward the challenging goal of fabricating high-quality CsPbI$_3$ films in an ambient environment. The salt contains a bulky [PPN]$^+$ cation, and a weakly-coordinating hydrophobic [TFSI]$^-$ anion was used to adjust the solid-state reaction process between DMAPbI$_3$ and Cs$_4$PbI$_6$. [PPN][TFSI] was added into the CsI, PbI$_2$, and DMAI precursor solution, and the film formation process was recorded by time-dependent morphological and crystallographic characterizations. The difference between films without (control) and with [PPN][TFSI] addition already appeared after drying at 100°C in N$_2$ (fig. S2), where the film containing [PPN][TFSI] shows heterogeneous agglomeration compared to the control film, which may be related to the interactions of [PPN][TFSI] with the precursor. Upon annealing at 180°C in the air, numerous tiny grains (~100 nm) are formed in the control film whereas the film where [PPN][TFSI] was included showed the presence of large domains (~250 nm) surrounded by small crystals (Fig. 1A). As the annealing progresses, the small grains of the control film grow and fuse together to form a continuous perovskite film at 12 min and with limited morphology changes between 12 and 15 min. Further prolonging the annealing to 40 min induces the phase transition of CsPbI$_3$ from the black phase to the yellow phase with the feature of poorly defined grain boundaries. This will be demonstrated and discussed below. The film containing [PPN][TFSI] undergoes a similar growth process; however, it takes up to 40 min to complete growth and shows much smoother and larger perovskite grains than the control film. This process was also observed at a macroscopic level using in situ optical microscopy (fig. S3). In contrast to the many small nuclei of the control film, the film with [PPN][TFSI] initially shows fewer but larger scattered nucleus clusters at the beginning. With constant heating, the crystals start to grow through large aggregates, small seed crystals, and large grains to the final dense film. In contrast, the control film demonstrates a faster crystal growth, and small-sized grains are eventually formed. The decelerated film-forming process in the presence of [PPN][TFSI] can also be identified by the color evolution of the perovskite films (fig. S4). It takes the film with [PPN][TFSI] twice as long as the control film (~8 min versus ~4 min) to turn black in the air, and the stability at 180°C is notably enhanced after the addition of [PPN][TFSI] (~150 min versus ~17 min). These phase evolutions

indicate that the introduction of [PPN][TFSI] retards the formation of both the black and yellow phases of CsPbI$_3$ films in the air.

To characterize the phase change during the formation of the CsPbI$_3$ films at 180°C, photoluminescence (PL) intensities were mapped over time (Fig. 1B). No obvious signals for black phases were detected at the initial stage of annealing. With the energy input increasing, the control film shows enhanced PL emission of black-phase CsPbI$_3$ with the maximum emission at 15 min. The black phase totally disappears after 40 min, which is ascribed to the degradation to the yellow phase and is in line with photographs (fig. S4). In contrast, slower formation of the black phase and an improved phase stability are demonstrated for the film with [PPN][TFSI], where the PL intensity progressively increases over time, and the black phase is sustained for a notably longer time (40 min). It is worth noting that the PL intensity of the final CsPbI$_3$ film is strengthened several times after the incorporation of [PPN][TFSI], indicating a high-quality film with decreased defect density (43).

Time-resolved x-ray diffraction (XRD) was collected for the CsPbI$_3$ films (Fig. 1C). The diffraction peaks were indexed into DMAPbI$_3$, C$_4$PbI$_6$, γ-DMA$_x$Cs$_{1-x}$PbI$_3$, and δ-CsPbI$_3$ (42). Both films exhibit only DMAPbI$_3$ (11.69°) and C$_4$PbI$_6$ (11.96°, 12.17°, and 28.55°) intermediate phases at the beginning of the annealing process. Whereafter, for the control film, the peak intensities of DMAPbI$_3$ and C$_4$PbI$_6$ gradually diminish and disappear at ~7 min. Meanwhile, the γ-DMA$_x$Cs$_{1-x}$PbI$_3$ perovskite phase starts to grow from 2 min. With the annealing time approaching 14 min, the γ phase begins degrading to the δ phase, and the total phase transition to δ phase (10.00° and 13.12°) was observed after 35 min. The constant heating process enables the partial volatilization of DMAI, which makes a decrease of the value of x in the composition of DMA$_x$Cs$_{1-x}$PbI$_3$, as confirmed by the peak position of γ-DMA$_x$Cs$_{1-x}$PbI$_3$ shifting from 14.28° to 14.33° and 28.75° to 28.89°. With the addition of [PPN][TFSI] (0.025 mol %), the characteristic peak representing pure [PPN][TFSI] can hardly be observed due to the low amount contained in the film (fig. S5). The time that the DMAPbI$_3$ and C$_4$PbI$_6$ intermediate phases are observed is also increased when [PPN][TFSI] is present (22 min versus 7 min), and the γ-DMA$_x$Cs$_{1-x}$PbI$_3$ phase forms later than that of the control film (3 min versus 2 min). After annealing for 150 min, the peak positions of γ-DMA$_x$Cs$_{1-x}$PbI$_3$ shifted to 14.37° and 28.93°, assigned to the characteristic peaks of pure-phase γ-CsPbI$_3$ without DMAI residuals. Meanwhile, [PPN][TFSI] mitigates the phase transition from γ to δ and increases the time to complete degradation from 35 to 200 min, which allows for ion exchange across the grain boundaries and further grain fusion into large grains. These crystallographic observations are consistent with the morphological and photophysical results (Fig. 1, A and B, and fig. S6). In addition, [PPN][TFSI] does not affect the crystal orientation as revealed by grazing-incidence wide-angle x-ray scattering (GIWAXS) (fig. S7). Both films show oriented growth in the deeper region of the film, reflected by more discrete diffraction arcs at q = 1.004 Å^{-1} with increasing the incident angle to 4.00°. It is noted that additional peaks at around q = 0.708 Å^{-1} and 0.922 Å^{-1} were observed in the control film, which correspond to the (011) and (012) planes of δ-phase CsPbI$_3$, respectively, implying the degradation of γ-CsPbI$_3$ (44).
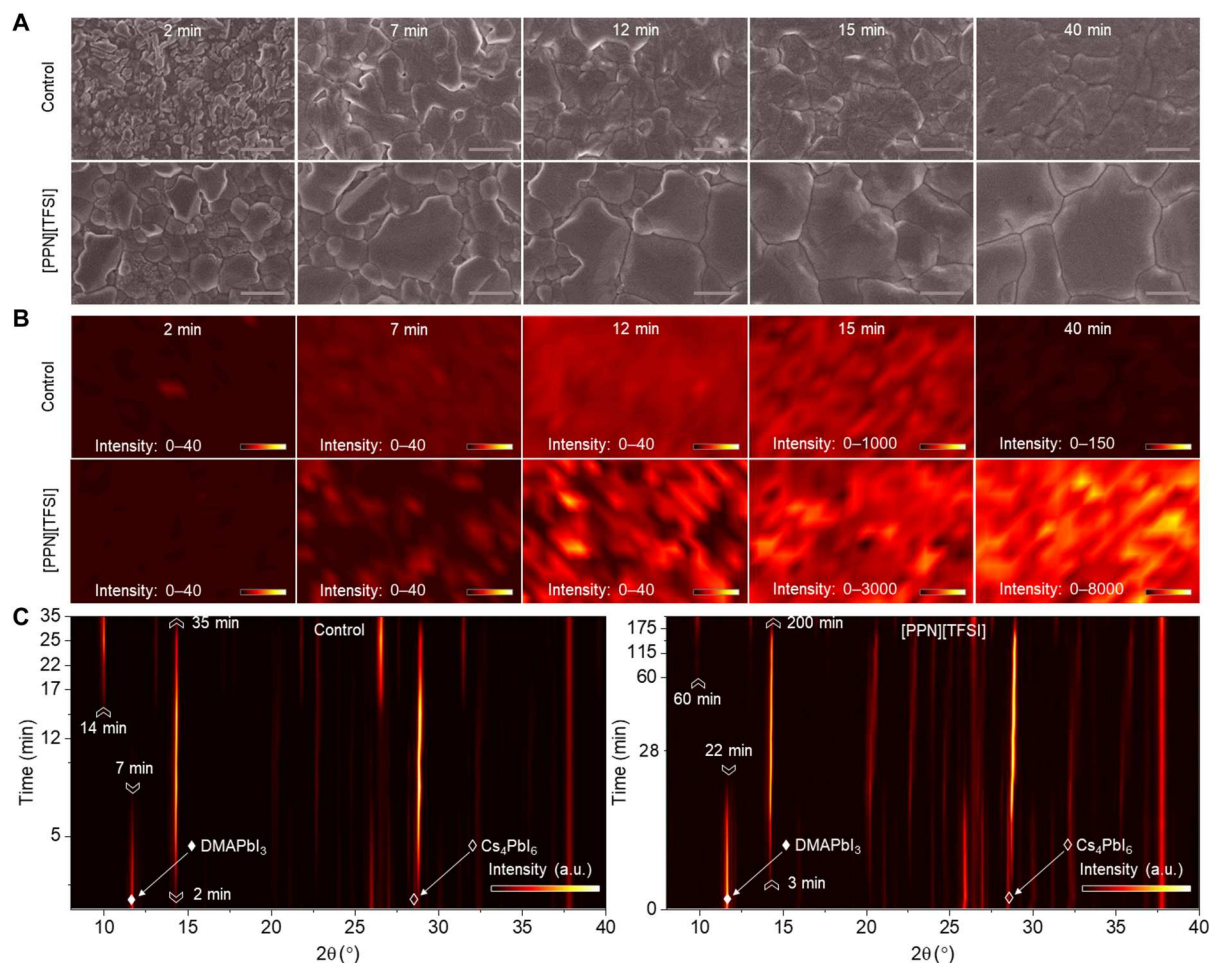
Fig. 1. Characterization of the formation of CsPbI$_3$ perovskite films. (**A**) Scanning electron microscopy (SEM) images of CsPbI$_3$ perovskite films without and with [PPN][TFSI] during the annealing process. Scale bars, 500 nm. (**B**) PL intensity maps for CsPbI$_3$ perovskite films without and with [PPN][TFSI] during the annealing process. Scale bars, 4 μm. (**C**) X-ray diffraction intensity as a function of diffraction angle and annealing time for CsPbI$_3$ perovskite films without and with [PPN][TFSI]. a.u., arbitrary unit.

Mechanism of the retarded solid-state reaction

To explore the origin of the role of the [PPN][TFSI], the molecular structure of [PPN][TFSI] was determined by single-crystal XRD (fig. S8 and data S1). The [PPN][TFSI] structure consists of the [PPN]$^+$ cation with the two triphenylphosphane groups shielding the iminium nitrogen. The two CF$_3$ groups in the [TFSI] anion are trans despite the high symmetry of the cation (45). The bond angles and distances in the cation and anion are within the expected range (45, 46). Examination of the packing reveals that the hydrogen bonding is generally strong, comparable with that found in salts containing an imidazolium cation with the same [TFSI]$^-$ anion. The shortest C-H—O bonds are in the range of 2.470 to 2.500 Å, and the shortest C-H—F distances are 2.530 to 2.613 Å (Fig. 2A). Interesting, there are relatively strong C-H—π interactions with the shortest distance being 2.736 Å (Fig. 2B). An F—F interaction is also present (2.896 Å). The nitrogen atom in the iminium center is not involved in any hydrogen bonding.

The reaction of [PPN][TFSI] with perovskite precursors CsI and PbI$_2$ was carried out with a 1:1:1 molar ratio in dimethyl sulfoxide (DMSO) to determine whether a chemical transformation could take place during the annealing process (fig. S9). [PPN][TFSI] crystallized from the DMSO solution independently, together with PbI$_2$·DMSO needle crystals, as evidenced by single-crystal XRD analysis (fig. S10), suggesting that no chemical reactions between [PPN][TFSI] and CsI/PbI$_2$ occur in DMSO solvent.

A further two model reactions were conducted in *N,N'*-dimethylformamide (DMF): (i) a three-component reaction between [PPN][TFSI], DMAI, and PbI$_2$ was performed by mixing the three components in a 1:1:1 molar ratio in DMF. A yellow solution is obtained from which yellow crystals were grown following slow evaporation of the solvent (fig. S11, A and B). The yellow crystals were characterized as [PPN][PbI$_3$] using single-crystal XRD analysis (fig. S12 and data S2 and S3), in which the [PPN] cation forms an ion pair with the PbI$_3$ anion. After complete evaporation of the DMF solvent, white crystals also formed (fig. S11B), which correspond to [DMA][TFSI], confirmed by nuclear magnetic resonance (NMR) spectroscopy following dissolution in D$_2$O. The ^{1}H NMR spectrum of the D$_2$O solution contains a peak at 2.73 parts per million (ppm), which corresponds to the N(CH$_3$)$_2$ protons in the DMA$^+$ cation (fig. S13A; note that the N-H protons undergo
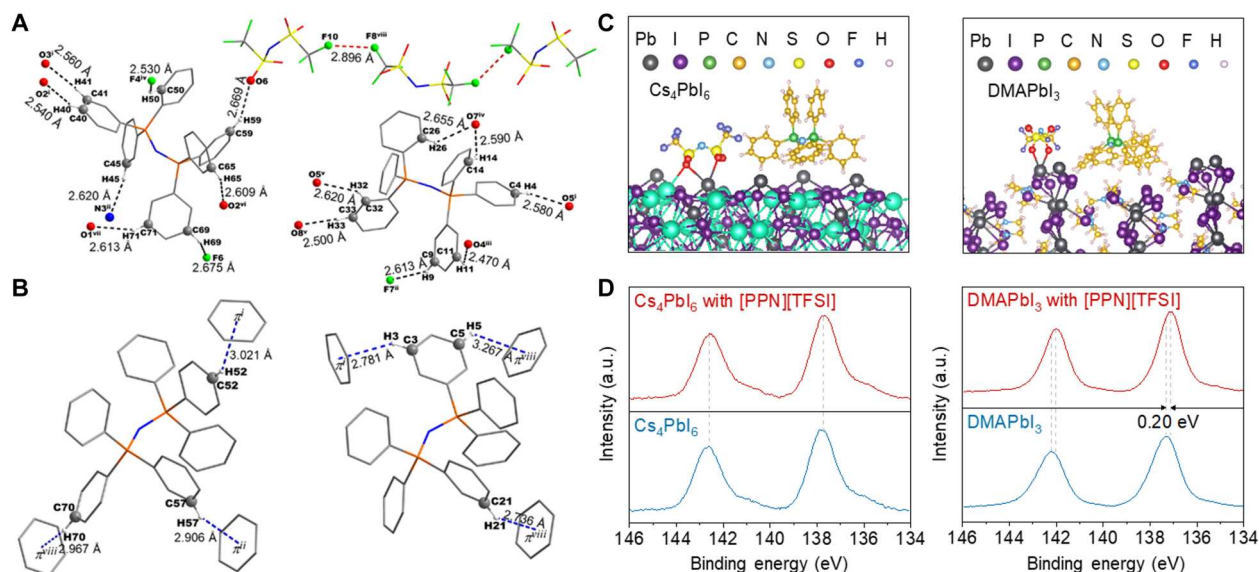
Fig. 2. Crystal structure of [PPN][TFSI] and its interaction with DMAPbI₃. (**A**) Molecular unit of [PPN][TFSI] with C-H—O/F hydrogen bonding. (**B**) Molecular structure of [PPN][TFSI] with C-H—π interactions. (**C**) Representative structures used for theoretical modeling on the interaction between [PPN][TFSI] and intermediate phases of Cs_4PbI_6 and $DMAPbI_3$. (**D**) XPS spectra of Pb 4f levels for Cs_4PbI_6 and $DMAPbI_3$ interacting with [PPN][TFSI].

exchange with D in the solvent and are therefore not observed) (*47*). The ^{19}F NMR spectrum a single peak at −79.19 ppm (fig. S13B), which is characteristic of the CF_3 groups in the $TFSI^-$ anion (*48*). (ii) A four-component reaction between [PPN][TFSI], DMAI, PbI_2, and CsI was also performed with each component in 1:1:1:1 molar ratio in DMF. As observed in the three-component reaction, [PPN]PbI_3 was formed (confirmed by single-crystal XRD analysis; fig. S14). CsI does not participate in the anion exchange process, although the crystal of [PPN]PbI_3 comprises a host-guest complex with DMF and H_2O solvate, i.e., [PPN][PbI_3]·H_2O·DMF. Note that the water solvate present in the crystal originates from water in the air, as the reactions were not conducted under an inert atmosphere. On the basis of the results from the model reactions, we believe both [PPN] cation and [TFSI] anion have strong interaction with the $DMAPbI_3$ intermediate phases, and [PPN][TFSI] may acts as phase-regulating additives together with these formed ion pairs during the film formation.

The interaction between [PPN][TFSI] and the intermediate phases was evaluated by theoretical modeling. The representative structures are shown in Fig. 2C. Accumulation of [PPN][TFSI] on the surfaces of the intermediate phase $DMAPbI_3$, preceding the perovskite formation, is energetically favorable with a calculated adsorption energy of −0.99 eV, which is lower than that of Cs_4PbI_6 (−0.9 eV). The higher adsorption energy of [PPN][TFSI] on the γ-phase $CsPbI_3$ is estimated to be −2.94 eV (fig. S15), explaining the tendency toward the final perovskite formation. X-ray photoelectron spectroscopy (XPS) was used to verify our theoretical observations (Fig. 2D). A shift of 0.22 eV in the Pb 4f peak was observed in the sample of $DMAPbI_3$ with [PPN][TFSI], whereas small change of 0.08 eV was observed in the Pb 4f peak for Cs_4PbI_6, indicating that the dominant interactions is between [PPN][TFSI] and the $DMAPbI_3$ intermediate phase. Thermogravimetric analysis (TGA) of the prepared γ-$DMA_xCs_{1-x}PbI_3$ sample with [PPN][TFSI] shows an upward shift of the inflection point

(230°C) compared to that of the control (200°C) as shown in fig. S16, demonstrating a retarded release of the DMAI component caused by the interaction of [PPN][TFSI] with $DMAPbI_3$. The main weight loss at around 460°C is assigned to the loss of the inorganic $CsPbI_3$ component.

The above analyses throughout the crystallization hint at the underlying mechanism for the high-quality growth of $CsPbI_3$ perovskite films (fig. S17). Consistent with a previous report (*42*), the initial films are composed of $DMAPbI_3$ and Cs_4PbI_6 intermediates, where the high-yield $DMAPbI_3$ is in the majority and has a higher crystallinity than the Cs_4PbI_6 (fig. S17). In the conventional film formation, the Cs_4PbI_6 crystals are initially randomly distributed around the $DMAPbI_3$ crystals. Their interaction occurs as the annealing process goes on and contributes to forming the final $CsPbI_3$ perovskite film at a relatively faster rate. By contrast, when [PPN][TFSI] is involved, it and the potentially formed ion pairs adsorbed on the surface of $DMAPbI_3$ grains, which hinders the reaction of $DMAPbI_3$ with Cs_4PbI_6. In the meantime, small $DMAPbI_3$ crystals grow and fuse together to form large grains, which is also reflected by the increased crystallinity of $DMAPbI_3$ (fig. S18) and the enlarged grain size of the film after annealing for 2 min (Fig. 1A and fig. S2). Under the constant annealing, the Cs_4PbI_6 starts to overcome the [PPN][TFSI] barrier and slowly reacts with $DMAPbI_3$ to trigger the phase transition from intermediate phases to perovskite. The [PPN][TFSI] remains at grain boundaries after the complete crystallization process owing to its high sublimation temperature (fig. S19). Therefore, [PPN][TFSI] greatly retards the solid-state reaction of the intermediates and slows down the growth of $CsPbI_3$ perovskite under high temperature in the air, which is beneficial for achieving denser, smoother, and larger-grain perovskite films.

Passivation effect of the [PPN][TFSI]

Density functional theory (DFT) simulations were performed to investigate the potential passivation effect of [PPN][TFSI] on CsPbI$_3$ perovskite. Occupation of [PPN][TFSI] on both CsI-terminated and PbI$_2$-terminated (001) surfaces was simulated, and both the cationic vacancies (Cs and Pb) and the anionic vacancies (I) were considered (Fig. 3, A to D; fig. S20; and table S1). The presence of [PPN][TFSI] on the perovskite surfaces substantially increases the formation energies of I$^-$, Cs$^+$, and Pb^{2+} surface vacancies. This makes their formation at the surfaces, interfaces, and grain boundaries largely unfavorable and therefore decreases their concentration, reducing the density of trap states due to point defects, which are known to be one of the major sources of efficiency losses in PSCs. As a result, the nonradiative electron-hole recombination losses are expected to be diminished, and PSC efficiency increased. In addition, from a device durability viewpoint, decreasing the concentration of surface vacancies is favorable for the kinetic stabilization of the perovskite layer because it diminishes the concentration of centers initiating the degradation process, thus extending the longevity of the resulting thin films. The PL spectra show an increased PL intensity and longer carrier lifetimes for the CsPbI$_3$ perovskite film containing [PPN][TFSI] (Fig. 3, E and F), which is in line with the passivation of defects and suppression of nonradiative recombination. The quantitative characterization of defect densities was estimated by the space charge–limited current (SCLC) method (47). As shown in Fig. 3 (G and H), the trap-filled limit voltage (V_{TFL}) is reduced to 0.83 V from 1.13 V with the assistance of [PPN][TFSI], corresponding to a decreased density of trap states from 4.94×10^{15} to 3.63×10^{15} cm^{-3}. Therefore, we have theoretically and experimentally demonstrated that the [PPN][TFSI] salt plays a positive role in suppressing the defect formation in CsPbI$_3$ perovskite films.

PV performance of PSCs and modules

The CsPbI$_3$-based solar cells with active area of 0.09 cm^2 were fabricated with the n-i-p architecture of fluorine-doped tin oxide (FTO)/SnO$_2$/perovskite/2,2',7,7'-tetrakis[N,N-di(4-methoxyphenyl)amino]-9,9'-spirobifluorene (Spiro-OMeTAD)/Au, as displayed in the cross-section scanning electron microscopy (SEM) image (Fig. 4A). The films and devices using [PPN][TFSI] with different concentrations were investigated (fig. S21 and table S2). The results indicate an optimal device performance at 0.025 mol % and reveal that [PPN][TFSI] improves the device performance by enhancing the open-circuit voltage (V_{OC}) and fill factor (FF), which originates from the increased film quality, the reduced defects, and the suppressed nonradiative recombination (fig. S22). The data obtained from the device exhibiting the best current density-voltage (J-V) characteristics are shown in Fig. 4B, exhibiting a PCE of 20.64% with a short-circuit current density (J_{SC}) of 20.91 mA cm^{-2}, a V_{OC} of 1.21 V, and an FF of 81.22%. The integrated J_{SC} value from external quantum efficiency (EQE) spectra (fig. S23) was calculated to be 20.30 mA cm^{-2}, well matched with that measured from the J-V curves (<3% discrepancy). The perovskite devices based on the CsPbI$_3$ film with [PPN][TFSI] show good reproducibility, with 85% of the devices achieving PCEs over 19% among 20 individual cells (fig. S24). The CsPbI$_3$-[PPN][TFSI]–based device also achieves a certified PCE up to 19.69% for the reverse sweep and 18.95% for the forward sweep (Fig. 4C and fig. S25), one of the highest certified PCEs with negligible hysteresis (table S3) (3, 49–51).

To evaluate the compatibility of [PPN][TFSI] with upscaling processes, CsPbI$_3$-based solar minimodules were fabricated with a size of 6.5 cm by 7 cm and eight subcells connected in series (Fig. 4D). The modules with a geometric FF of 90% show a high PCE of 16.89% with an active area of 28.17 cm^2 and an efficiency
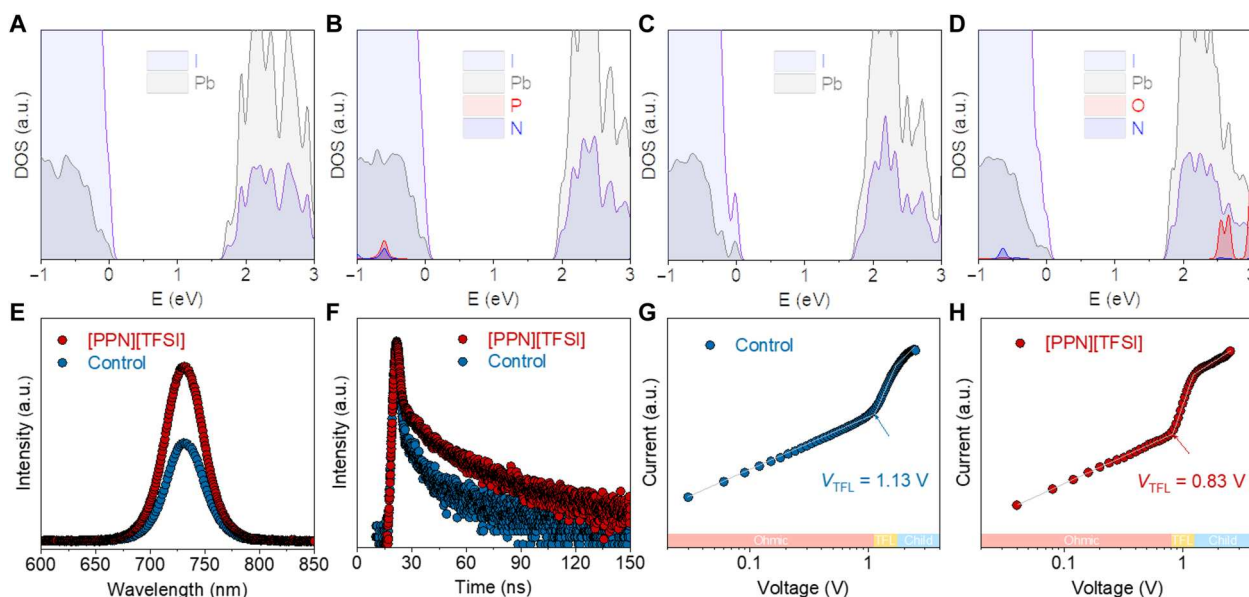
Fig. 3. Passivation Effect of [PPN][TFSI] on CsPbI$_3$ perovskite films. Partial density of states (PDOS) of the (**A**) control and (**B**) [PPN][TFSI]-incorporated CsPbI$_3$ perovskite with I vacancy on PbI-terminated surface. PDOS of the (**C**) control and (**D**) [PPN][TFSI]-incorporated CsPbI$_3$ perovskite with Pb vacancy on PbI-terminated surface. (**E**) PL spectra of CsPbI$_3$ perovskite films on glass substrates with an excitation wavelength of 450 nm. (**F**) PL decay curves with an excitation wavelength of 450 nm, indicating a longer carrier lifetime for the film with [PPN][TFSI]. Dark current curves of the SCLC model for CsPbI$_3$ perovskite films (**G**) without and (**H**) with [PPN][TFSI]. TFL, trap-filled limit.
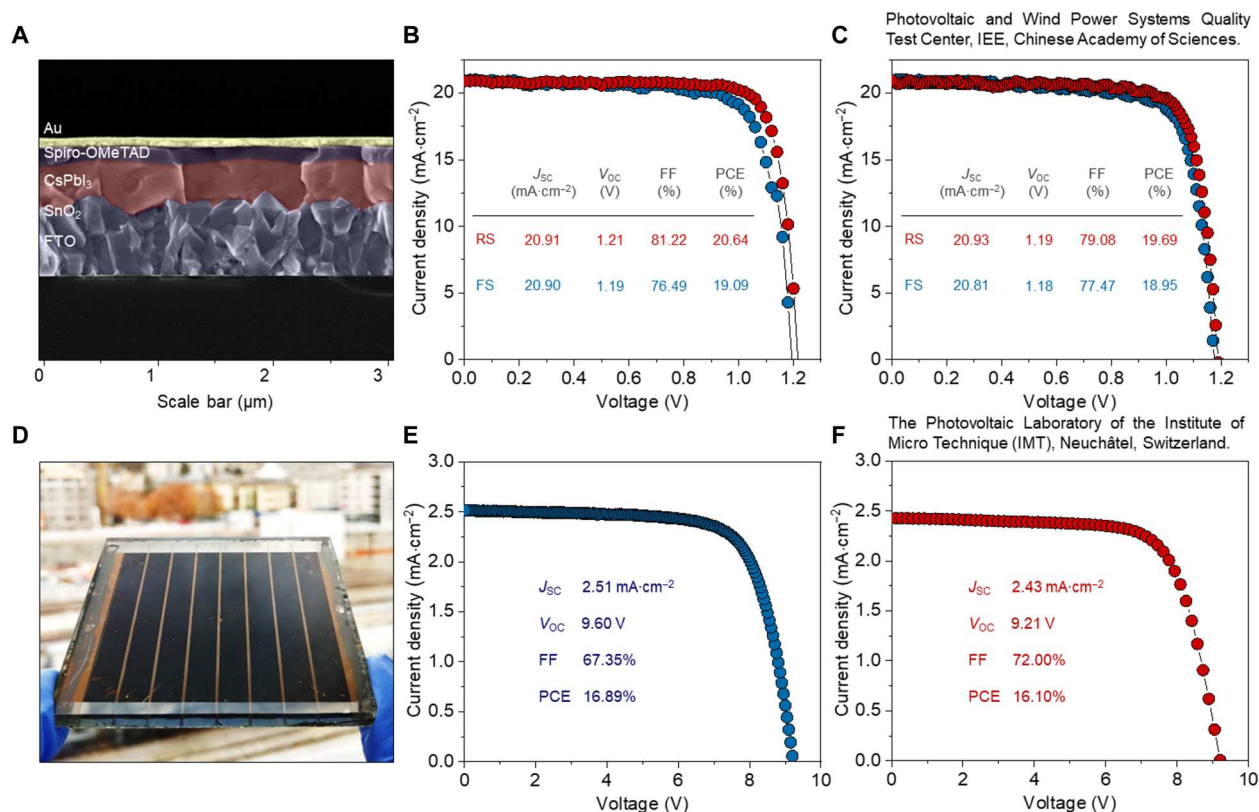
Fig. 4. Device performance. (**A**) Cross-section SEM image showing the device structure. (**B**) *J-V* characteristics of the champion cell. (**C**) *J-V* curves of the device certified at Photovoltaic and Wind Power Systems Quality Test Center, IEE, Chinese Academy of Sciences. (**D**) Photograph of the CsPbI$_3$ perovskite solar minimodule. (**E**) *J-V* characteristics of the best minimodule. (**F**) *J-V* curve of the minimodule was verified at the Photovoltaic Laboratory of the Institute of Micro Technique (IMT), Neuchatel, Switzerland. PCE, power conversion efficiency; FF, fill factor; J_{SC}, short-circuit current density; V_{OC}, open-circuit voltage; Spiro-OMeTAD, 2,2',7,7'-tetrakis[*N,N*-di(4-methox-yphenyl)amino]-9,9'-spirobifluorene. FTO, fluorine-doped tin oxide.

of 15.20% with an aperture area of 31.30 cm^2 (Fig. 4E), which is the highest efficiency for inorganic perovskite solar modules reported so far (table S4) (*33, 36, 37*). Moreover, the best-performing module was sent for verification by the PV laboratory of the Institute of Micro Technique, Neuchâtel, Switzerland, and the stabilized active area and aperture efficiencies were determined to be 16.10 and 14.49%, respectively (Fig. 4F and fig. S26). The implementation of large-area applications is ascribed to the high quality and uniformity of CsPbI$_3$ films by introducing [PPN][TFSI].

Theoretical simulations were performed to explore the effect of [PPN][TFSI] on the stability of CsPbI$_3$ perovskite. The adsorption model of [PPN][TFSI] on both δ-phase CsPbI$_3$ and γ-phase CsPbI$_3$ was established (fig. S15). Adsorption of [PPN][TFSI] on the surface of δ-phase of CsPbI$_3$ is much less energetically favorable (ΔE_{ads} = −0.61 eV) in contrast to adsorption on the surface of γ-phase CsPbI$_3$ (ΔE_{ads} = −2.94 eV), particularly, due to the formation of the strong Pb-O contacts (2.6 to 2.9 Å) with the [TFSI]$^-$ anion, thus stabilizing the γ-phase. The potential Pb-O interactions were further confirmed by the XPS spectra shown in fig. S27, where both O 1*s* of [PPN][TFSI] and Pb 4*f* of CsPbI$_3$ shifted to lower energy after interaction. The degradation from the γ-phase to the δ-phase was also simulated (Fig. 5, A and B). Without the presence of [PPN][TFSI], the δ-phase surface is stabilized with respect to the γ-phase surface by 0.13 eV per stoichiometric unit, while in

the presence of [PPN][TFSI] (1/2 monolayer coverage), this value is reduced to 0.06 eV per stoichiometric unit, showing the effect of [PPN][TFSI] on the stabilization of γ-phase. This is reflected in the long-term stabilities of the unencapsulated small-area devices (Fig. 5, C and D). The CsPbI$_3$-[PPN][TFSI] devices retain 82 and 72% of their original PCEs after 1000 hours of storage in an ambient of 20 to 30% relative humidity (RH) and constant heating at 85°C in N$_2$ atmosphere, respectively, whereas the pure CsPbI$_3$ devices drop to 63 and 58% of their original performance under the same ambient and thermal condition, respectively. The use of the standard doped Spiro-OMeTAD could potentially accelerate the device degradation under humid air (fig. S28) due to the hygroscopic nature of the dopants (*37*). In addition, the long-term operational stability of the unencapsulated devices was traced under continuous 1-sun irradiation (100 mW cm^{-2}, AM1.5G, 25°C, RH of ~2%) with N$_2$ flow at the maximum power point (MPP). The CsPbI$_3$-[PPN][TFSI] device maintains about 88% of its initial PCE after 1000 hours of light soaking (Fig. 5E), overwhelming that of 53% for the pure CsPbI$_3$ device.

DISCUSSION
We have shown that the addition of [PPN][TFSI] IL retards the high-temperature solid-state reaction of the intermediates formed
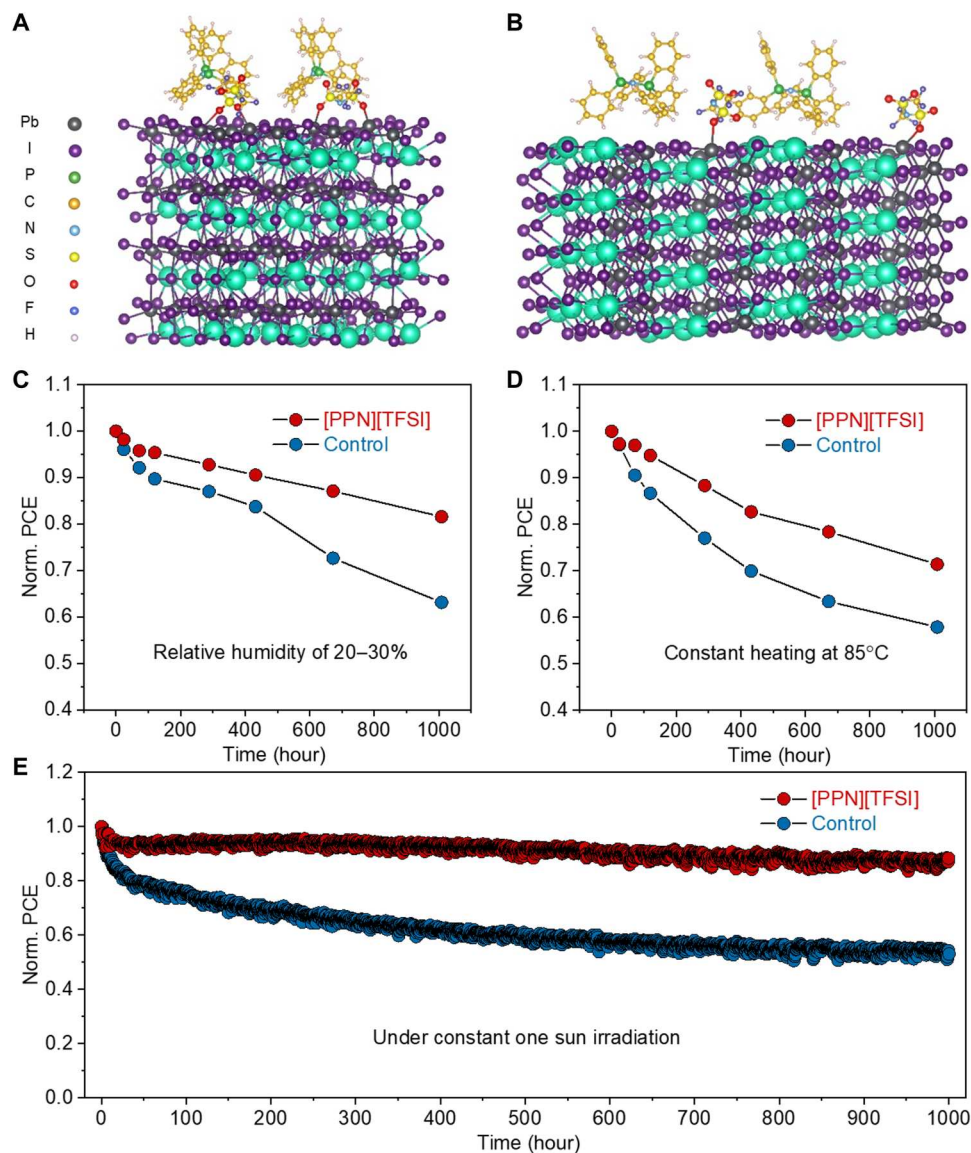
Fig. 5. Stability. [PPN][TFSI] IL adsorbed on surfaces of (**A**) γ-phase and (**B**) δ-phase CsPbI$_3$. (**C**) Humidity stability of CsPbI$_3$ PSCs in ambient at RT. (**D**) Thermal stability of CsPbI$_3$ PSCs in N$_2$ atmosphere. (**E**) Long-term MPP tracking of the unencapsulated devices under AM1.5G irradiation.

from the perovskite precursors and enables the preparation of high-quality and stable CsPbI$_3$ perovskite films on a large scale. The [PPN][TFSI] slows the formation of γ-CsPbI$_3$ by interacting with the DMAPbI$_3$ intermediate and controlling the ion exchange rate, thus allowing the formation of large crystal grains. The defect density of the prepared CsPbI$_3$ films is further reduced by effective passivation with [PPN][TFSI]. The [PPN][TFSI] salt increases the energy barrier of transition from γ-phase to δ-phase and thus enhances the structural and environmental stability of CsPbI$_3$ perovskite. The optimized devices realize PCEs of 20.64% (certified 19.69%) and 16.89% for small-area (0.09 cm^2) PSCs and large-area (28.17 cm^2) modules, respectively. This strategy could be relevant to other all-inorganic PSCs and would contribute to their further development of large-scale applications.

MATERIALS AND METHODS
Materials
CsI (99.99%) and DMAI (99%) were purchased from Xi'an Polymer Light Technology. PbI$_2$ (99.99%) was purchased from Tokyo Chemical Industry. DMSO (99.9%), ethyl acetate (99.8%), TFSI lithium salt (Li[TFSI]; 99.0%), chlorobenzene (99.8%), and 4-*tert*-butylpyridine (98%) were purchased from Sigma-Aldrich. Spiro-OMeTAD (99.8%) was purchased from Borun New Material Technology. Acetonitrile (99%) was purchased from Aladdin. All reagents were used as received without further purification.

Synthesis of [PPN][TFSI]
A mixture of PPN chloride (574 mg, 1.0 mmol) and Li[TFSI] (288 mg, 1.0 mmol) in water (10.0 ml) was stirred at RT overnight. The solid was filtrated and washed with water (4 × 10 ml) followed by drying under vacuum to give the product a yield of 794 mg, 97%.

X-ray crystallography

Single crystals suitable for XRD analysis were obtained directly from a saturated solution of [PPN][TFSI] in DMF by slow evaporation at RT over 5 days. A colorless plate-shaped crystal with dimensions 0.19 mm by 0.09 mm by 0.02 mm was mounted. Data were collected using a SuperNova, Dual, Cu at home/near, Atlas diffractometer operating at $T = 140.01(10)$ K. Data were measured using w scans using Cu Kα radiation. The diffraction pattern was indexed, and the total number of runs and images was based on the strategy calculation from the program CrysAlisPro (Rigaku, V1.171.41.89a, 2020) (52). The maximum resolution achieved was $Q = 72.603^°$ (0.81 Å). The diffraction pattern was indexed, and the total number of runs and images was based on the strategy calculation from the program CrysAlisPro (Rigaku, V1.171.41.89a, 2020). The unit cell was refined using CrysAlisPro (Rigaku, V1.171.41.89a, 2020) on 25808 reflections, 42% of the observed reflections (52).

Data reduction, scaling, and absorption corrections were performed using CrysAlisPro (Rigaku, V1.171.41.89a, 2020) (52). The final completeness is 99.90% out to 72.603° in Q. A Gaussian absorption correction was performed using CrysAlisPro 1.171.41.89a (Rigaku Oxford Diffraction, 2020) (52) Numerical absorption correction is based on Gaussian integration over a multi-faceted crystal model. Empirical absorption correction was performed using spherical harmonics as implemented in SCALE3 ABSPACK scaling algorithm. The absorption coefficient m of this material is 2.770 mm^{-1} at this wavelength ($l = 1.54184$ Å), and the minimum and maximum transmissions are 0.601 and 1.000. The structure was solved, and the space group $P2_1/c$ (# 14) was determined by the SHELXT (53) 2018/2 structure solution program using dual methods by using Olex2 (54) and refined by full matrix least squares minimisation on F^2 using version 2018/3 of SHELXL 2018/3 (55). All nonhydrogen atoms were refined anisotropically. Hydrogen atom positions were calculated geometrically and refined using the riding model. The value of Z' is 2. This means that there are two independent molecules in the asymmetric unit. Crystallographic and refinement data are summarized in data S1 and tables S1 to S7. The Cambridge Crystallographic Data Centre (CCDC) number 2201978 for compound [PPN][TFSI] contains the supplementary crystallographic data for this paper. These data can be obtained, free of charge, from the CCDC via www.ccdc.cam.ac.uk/structures.

Device fabrication

The electron transport layers were first deposited on FTO substrates precleaned by detergent, deionized water, acetone, and isopropanol. As our previous report (31), The TiO$_2$ layer was prepared by atomic layer deposition method, and the SnO$_2$ colloidal solution was then spin-coated on it at 3000 rpm for 30 s, followed by annealing at 180°C for 30 min. The 1.43 M DMA$_x$Cs$_{1-x}$PbI$_3$ precursor solution was prepared by dissolving CsI, DMAI, and PbI$_2$, with a 1:1:1 molar ratio in DMSO. The precursor solution was deposited at 1000 rpm for 10 s and 4000 rpm for 30 s in the glovebox for better uniformity. At 20 s of the second step, 300 μl of ethyl acetate was dropped on the spinning films. The substrates were annealed at 100°C for 10 min and 180°C for 20 min in the ambient to obtain control films. For the target films, the only difference is that 0.025 mol % [PPN][TFSI] was added into the perovskite precursor solution. Hole transport material (HTM) solution was prepared by dissolving 72.3 mg of Spiro-OMeTAD in 1 ml of chlorobenzene with the addition of 46.3 μl of Li[TFSI]/acetonitrile solution (1.8 M) with 1.645 ml of 4-*tert*-butylpyridine/ml. The HTM solution was spin-coated at 3000 rpm for 30 s. The devices were completed by thermally evaporating a 60-nm-thick Au electrode under a high vacuum.

Computational details

The simulations are performed within the DFT using Perdew-Burke-Ernzerhof (56) density functional, as implemented in the CP2K code (57). DZVP-MOLOPT basis set (58) and plane wave auxiliary basis set with the 600-rydberg cutoff are used for the description of the wave function and the charge density, respectively. The core region is described with the norm-conserving Goedecker-Teter-Hutter (59) pseudopotentials, the number of electrons for Cs, I/F, S/O, N/P, Pb/C, and H placed in the valence region being equal to 9, 7, 6, 5, 4, and 1, respectively. Because of the large extent of the unit cells, Γ-point is used for the sampling of the reciprocal space. The considered nonperovskite surface slabs were constructed from the yellow δ-phase of CsPbI$_3$ having an orthorhombic *Pnam* space group, the intermediate phase Cs$_4$PbI$_6$ of rhombohedral *R*-3*c* group, and layered δ-phase like of hexagonal *P*63/*mmc* space group. All the used structures are fully relaxed. The visualization is accomplished using VESTA software (60).

Characterization

XRD was performed by Rigaku x-ray diffractometer with Cu Kα (1.5418 Å) x-ray. The PL spectra and PL decays were recorded by marine optical microfiber spectrometer (Perkin LS-55) with an excitation laser at 450 nm. SEM images were obtained by Hitachi S-4800 field emission scanning electron microscope. The GIWAXS was measured at beamline BL19B2 of SPring-8 with PILATUS 300 K 2D x-ray detectors with a Huber diffractometer and photon energy of 12.39 keV (1.0 Å). TGA data were collected using TGA/DSC1 from Mettler Toledo. XPS was conducted in the N$_2$ by Thermo VG Scientific ESCALAB 250. The micro-PL maps were obtained using a confocal Raman scanning microscope (Witec), a digital silicon charge-coupled device linear array detector, and a 355-nm laser. The *J-V* characteristics of the PSCs were measured in ambient at 25°C with an RH of ~20% under an AM1.5G illumination connected to a digital source meter (Keithley 2400). A non-reflective metal mask defined the device's effective area as 0.09 and 31.30 cm^2 for small cells and large module, respectively. *J-V* curves were obtained from 1.3 to −0.1 V at a scan rate of 244 mV/s and from −0.1 to 1.3 V with a scan rate of 141 mV/s at RT in the air, where no preconditioning of the device before characterization. EQE was characterized by the Enlitech (Taiwan) Technology measurement system, which was calibrated with a silicon solar cell. The MPP tracing test was conducted under light-emitting diode illumination of 100 mW cm^{-2} at 25°C, and the devices were flushed with an N$_2$ flow.

Supplementary Materials

This PDF file includes:
Figs. S1 to S28
Tables S1 to S4
Legends for data S1 to S3
References

Other Supplementary Material for this manuscript includes the following:
Data S1 to S3

REFERENCES AND NOTES

1. R. J. Sutton, G. E. Eperon, L. Miranda, E. S. Parrott, B. A. Kamino, J. B. Patel, M. T. Hörantner, M. B. Johnston, A. A. Haghighirad, D. T. Moore, H. J. Snaith, Bandgap-tunable cesium lead halide perovskites with high thermal stability for efficient solar cells. *Adv. Energy Mater.* **6**, 1502458 (2016).

2. P. Wang, X. Zhang, Y. Zhou, Q. Jiang, Q. Ye, Z. Chu, X. Li, X. Yang, Z. Yin, J. You, Solvent-controlled growth of inorganic perovskite films in dry environment for efficient and stable solar cells. *Nat. Commun.* **9**, 2225 (2018).

3. Y. Wang, M. I. Dar, L. K. Ono, T. Zhang, M. Kan, Y. Li, L. Zhang, X. Wang, Y. Yang, X. Gao, Y. Qi, M. Grätzel, Y. Zhao, Thermodynamically stabilized β-CsPbI₃-based perovskite solar cells with efficiencies >18%. *Science* **365**, 591–595 (2019).

4. C. C. Stoumpos, M. G. Kanatzidis, Halide perovskites: Poor man's high-performance semiconductors. *Adv. Mater.* **28**, 5778–5793 (2016).

5. J. Li, C. C. Stoumpos, G. G. Trimarchi, I. Chung, L. Mao, M. Chen, M. R. Wasielewski, L. Wang, M. G. Kanatzidis, Air-stable direct bandgap perovskite semiconductors: All-inorganic tin-based heteroleptic halides AₓSnClᵧI₂ (A = Cs, Rb). *Chem. Mater.* **30**, 4847–4856 (2018).

6. Z. Li, F. Zhou, Q. Wang, L. Ding, Z. Jin, Approaches for thermodynamically stabilized CsPbI₃ solar cells. *Nano Energy* **71**, 104634 (2020).

7. Y. Wang, Y. Chen, T. Zhang, X. Wang, Y. Zhao, Chemically stable black phase CsPbI₃ inorganic perovskites for high-efficiency photovoltaics. *Adv. Mater.* **32**, 2001025 (2020).

8. B. Yu, J. Shi, S. Tan, Y. Cui, W. Zhao, H. Wu, Y. Luo, D. Li, Q. Meng, Efficient (>20%) and stable all-inorganic cesium lead triiodide solar cell enabled by thiocyanate molten salts. *Angew. Chem. Int. Ed.* **60**, 13436–13443 (2021).

9. X. Gu, W. Xiang, Q. Tian, S. Liu, Rational surface-defect control via designed passivation for high-efficiency inorganic perovskite solar cells. *Angew. Chem. Int. Ed.* **60**, 23164–23170 (2021).

10. K. Wang, Z. Jin, L. Liang, H. Bian, D. Bai, H. Wang, J. Zhang, Q. Wang, S. Liu, All-inorganic cesium lead iodide perovskite solar cells with stabilized efficiency beyond 15%. *Nat. Commun.* **9**, 4544 (2018).

11. C. Liu, Y. Yang, O. A. Syzgantseva, Y. Ding, M. A. Syzgantseva, X. Zhang, A. M. Asiri, S. Dai, M. K. Nazeeruddin, α-CsPbI₃ bilayers via one-step deposition for efficient and stable all-inorganic perovskite solar cells. *Adv. Mater.* **32**, 2002632 (2020).

12. T. Liu, J. Zhang, M. Qin, X. Wu, F. Li, X. Lu, Z. Zhu, A. K.-Y. Jen, Modifying surface termination of CsPbI₃ grain boundaries by 2D perovskite layer for efficient and stable photovoltaics. *Adv. Funct. Mater.* **31**, 2009515 (2021).

13. Z. Xu, L. Li, X. Dong, D. Lu, R. Wang, W.-J. Yin, Y. Liu, CsPbI₃-based phase-stable 2D ruddlesden-popper perovskites for efficient solar cells. *Nano Lett.* **22**, 2874–2880 (2022).

14. T. Liu, J. Zhang, X. Wu, H. Liu, F. Li, X. Deng, F. Lin, X. Li, Z. Zhu, A. K.-Y. Jen, Interfacial modification through a multifunctional molecule for inorganic perovskite solar cells with over 18% efficiency. *Solar RRL* **4**, 2000205 (2020).

15. X. Zhao, T. Liu, Q. C. Burlingame, T. Liu, R. Holley, G. Cheng, N. Yao, F. Gao, Y.-L. Loo, Accelerated aging of all-inorganic, interface-stabilized perovskite solar cells. *Science* **377**, 307–310 (2022).

16. C. Yan, Z. Li, Y. Sun, J. Zhao, X. Huang, J. Yang, Z. Ci, L. Ding, Z. Jin, Decreasing energy loss and optimizing band alignment for high performance CsPbI₃ solar cells through guanidine hydrobromide post-treatment. *J. Mater. Chem. A* **8**, 10346–10353 (2020).

17. A. Marronnier, G. Roma, S. Boyer-Richard, L. Pedesseau, J.-M. Jancu, Y. Bonnassieux, C. Katan, C. C. Stoumpos, M. G. Kanatzidis, J. Even, Anharmonicity and disorder in the black phases of cesium lead iodide used for stable inorganic perovskite solar cells. *ACS Nano* **12**, 3477–3486 (2018).

18. W. Xiang, Z. Wang, D. J. Kubicki, X. Wang, W. Tress, J. Luo, J. Zhang, A. Hofstetter, L. Zhang, L. Emsley, M. Grätzel, A. Hagfeldt, Ba-induced phase segregation and band gap reduction in mixed-halide inorganic perovskite solar cells. *Nat. Commun.* **10**, 4686 (2019).

19. Q. Ye, F. Ma, Y. Zhao, S. Yu, Z. Chu, P. Gao, X. Zhang, J. You, Stabilizing γ-CsPbI₃ perovskite via phenylethylammonium for efficient solar cells with open-circuit voltage over 1.3 V. *Small* **16**, 2005246 (2020).

20. J. Li, Q. Yu, Y. He, C. C. Stoumpos, G. Niu, G. G. Trimarchi, H. Guo, G. Dong, D. Wang, L. Wang, M. G. Kanatzidis, Cs₂PbI₂Cl₂, all-inorganic two-dimensional Ruddlesden–Popper mixed halide perovskite with optoelectronic response. *J. Am. Chem. Soc.* **140**, 11085–11090 (2018).

21. J. Zhang, Z. Wang, A. Mishra, M. Yu, M. Shasti, W. Tress, D. J. Kubicki, C. E. Avalos, H. Lu, Y. Liu, B. I. Carlsen, A. Agarwalla, Z. Wang, W. Xiang, L. Emsley, Z. Zhang, M. Grätzel, W. Guo, A. Hagfeldt, Intermediate phase enhances inorganic perovskite and metal oxide interface for efficient photovoltaics. *Joule* **4**, 222–234 (2020).

22. W. Xiang, J. Zhang, S. Liu, S. Albrecht, A. Hagfeldt, Z. Wang, Intermediate phase engineering of halide perovskites for photovoltaics. *Joule* **6**, 315–339 (2022).

23. Y. Du, Q. Tian, X. Chang, J. Fang, X. Gu, X. He, X. Ren, K. Zhao, S. Liu, Ionic liquid treatment for highest-efficiency ambient printed stable all-inorganic CsPbI₃ perovskite solar cells. *Adv. Mater.* **34**, e2106750 (2022).

24. Z. Wang, J. Zhang, W. Guo, W. Xiang, A. Hagfeldt, Formation and stabilization of inorganic halide perovskites for photovoltaics. *Matter* **4**, 528–551 (2021).

25. B. Zhao, S.-F. Jin, S. Huang, N. Liu, J.-Y. Ma, D.-J. Xue, Q. Han, J. Ding, Q.-Q. Ge, Y. Feng, J.-S. Hu, Thermodynamically stable orthorhombic γ-CsPbI₃ thin films for high-performance photovoltaics. *J. Am. Chem. Soc.* **140**, 11716–11725 (2018).

26. W. Ke, I. Spanopoulos, C. C. Stoumpos, M. G. Kanatzidis, Myths and reality of HPbI₃ in halide perovskite solar cells. *Nat. Commun.* **9**, 4785 (2018).

27. Y. Wang, X. Liu, T. Zhang, X. Wang, M. Kan, J. Shi, Y. Zhao, The role of dimethylammonium iodide in CsPbI₃ perovskite fabrication: Additive or dopant? *Angew. Chem. Int. Ed.* **58**, 16691–16696 (2019).

28. K. Wang, C. Gao, Z. Xu, Q. Tian, X. Gu, L. Zhang, S. Zhang, K. Zhao, S. Liu, In-situ hot oxygen cleansing and passivation for all-inorganic perovskite solar cells deposited in ambient at breakthrough 19% efficiency. *Adv. Funct. Mater.* **31**, 2101568 (2021).

29. L. Liang, Z. Li, F. Zhou, Q. Wang, H. Zhang, Z. Xu, L. Ding, S. Liu, Z. Jin, The humidity-insensitive fabrication of efficient CsPbI₃ solar cells in ambient air. *J. Mater. Chem. A* **7**, 26776–26784 (2019).

30. F. Huang, A. R. Pascoe, W.-Q. Wu, Z. Ku, Y. Peng, J. Zhong, R. A. Caruso, Y.-B. Cheng, Effect of the microstructure of the functional layers on the efficiency of perovskite solar cells. *Adv. Mater.* **29**, 1601715 (2017).

31. X. Sun, Z. Shao, Z. Li, D. Liu, C. Gao, C. Chen, B. Zhang, L. Hao, Q. Zhao, Y. Li, X. Wang, Y. Lu, X. Wang, G. Cui, S. Pang, Highly efficient CsPbI₃/Cs₁₋ₓDMAₓPbI₃ bulk heterojunction perovskite solar cell. *Joule* **6**, 850–860 (2022).

32. L. Liang, H. Luo, J. Hu, H. Li, P. Gao, Efficient perovskite solar cells by reducing interface-mediated recombination: A bulky amine approach. *Adv. Energy Mater.* **10**, 2000197 (2020).

33. J. H. Heo, F. Zhang, J. K. Park, H. Joon Lee, D. S. Lee, S. J. Heo, J. M. Luther, J. J. Berry, K. Zhu, S. H. Im, Surface engineering with oxidized Ti₃C₂Tₓ MXene enables efficient and stable p-i-n-structured CsPbI₃ perovskite solar cells. *Joule* **6**, 1672–1688 (2022).

34. J. H. Heo, F. Zhang, C. Xiao, S. J. Heo, J. K. Park, J. J. Berry, K. Zhu, S. H. Im, Efficient and stable graded CsPbI₃₋ₓBrₓ perovskite solar cells and submodules by orthogonal processable spray coating. *Joule* **5**, 481–494 (2021).

35. R. Chen, Y. Hui, B. Wu, Y. Wang, X. Huang, Z. Xu, P. Ruan, W. Zhang, F. Cheng, W. Zhang, J. Yin, J. Li, N. Zheng, Moisture-tolerant and high-quality α-CsPbI₃ films for efficient and stable perovskite solar modules. *J. Mater. Chem. A* **8**, 9597–9606 (2020).

36. R. Montecucco, E. Quadrivi, R. Po, G. Grancini, All-inorganic cesium-based hybrid perovskites for efficient and stable solar cells and modules. *Adv. Energy Mater.* **11**, 2100672 (2021).

37. C. Liu, C. Igci, Y. Yang, O. A. Syzgantseva, M. A. Syzgantseva, K. Rakstys, H. Kanda, N. Shibayama, B. Ding, X. Zhang, V. Jankauskas, Y. Ding, S. Dai, P. J. Dyson, M. K. Nazeeruddin, Dopant-free hole transport materials afford efficient and stable inorganic perovskite solar cells and modules. *Angew. Chem. Int. Ed.* **60**, 20489–20497 (2021).

38. S. Bai, P. Da, C. Li, Z. Wang, Z. Yuan, F. Fu, M. Kawecki, X. Liu, N. Sakai, J. T.-W. Wang, S. Huettner, S. Buecheler, M. Fahlman, F. Gao, H. J. Snaith, Planar perovskite solar cells with long-term stability using ionic liquid additives. *Nature* **571**, 245–250 (2019).

39. Y.-H. Lin, N. Sakai, P. Da, J. Wu, H. C. Sansom, A. J. Ramadan, S. Mahesh, J. Liu, R. D. J. Oliver, J. Lim, L. Aspitarte, K. Sharma, P. K. Madhu, A. B. Morales-Vilches, P. K. Nayak, S. Bai, F. Gao, C. R. M. Grovenor, M. B. Johnston, J. G. Labram, J. R. Durrant, J. M. Ball, B. Wenger, B. Stannowski, H. J. Snaith, A piperidinium salt stabilizes efficient metal-halide perovskite solar cells. *Science* **369**, 96–102 (2020).

40. N. Yan, Z. Fei, R. Scopelliti, G. Laurenczy, Y. Kou, P. J. Dyson, Crystallisation of inorganic salts containing 18-crown-6 from ionic liquids. *Inorganica Chim. Acta* **363**, 504–508 (2010).

41. D. Prodius, A.-V. Mudring, Rare earth metal-containing ionic liquids. *Coord. Chem. Rev.* **363**, 1–16 (2018).

42. H. Meng, Z. Shao, L. Wang, Z. Li, R. Liu, Y. Fan, G. Cui, S. Pang, Chemical composition and phase evolution in DMAI-derived inorganic perovskite solar cells. *ACS Energy Lett.* **5**, 263–270 (2020).

43. C. Liu, Y. Yang, K. Rakstys, A. Mahata, M. Franckevicius, E. Mosconi, R. Skackauskaite, B. Ding, K. G. Brooks, O. J. Usiobo, J.-N. Audinot, H. Kanda, S. Driukas, G. Kavaliauskaite, V. Gulbinas, M. Dessimoz, V. Getautis, F. De Angelis, Y. Ding, S. Dai, P. J. Dyson, M. K. Nazeeruddin, Tuning structural isomers of phenylenediammonium to afford efficient and stable perovskite solar cells and modules. *Nat. Commun.* **12**, 6394 (2021).

44. K. Choi, D. H. Lee, W. Jung, S. Kim, S. H. Kim, D. Lee, S. Song, T. Park, 3D interaction of Zwitterions for highly stable and efficient inorganic CsPbI₃ solar cells. *Adv. Funct. Mater.* **32**, 2112027 (2022).

45. J. D. Holbrey, W. M. Reichert, R. D. Rogers, Crystal structures of imidazolium Bis(Trifluoro-methanesulfonyl)Imide 'Ionic liquid' salts: The first organic salt with a *cis*-TFSI anion conformation. *Dalton Trans.*, 2267–2271 (2004).

46. A. R. Choudhury, N. Winterton, A. Steiner, A. I. Cooper, K. A. Johnson, In situ crystallization of low-melting ionic liquids. *J. Am. Chem. Soc.* **127**, 16792–16793 (2005).

47. W. M. J. Franssen, B. J. Bruijnaers, V. H. L. Portengen, A. P. M. Kentgens, Dimethylammonium incorporation in lead acetate based MAPbI₃ perovskite solar cells. *ChemPhysChem* **19**, 3107–3115 (2018).

48. S. Zhang, T. Xiao, F. F. Tirani, R. Scopelliti, M. K. Nazeeruddin, D. Zhu, P. J. Dyson, Z. Fei, The chemistry of the passivation mechanism of perovskite films with ionic liquids. *Inorg. Chem.* **61**, 5010–5016 (2022).

49. S. Tan, B. Yu, Y. Cui, F. Meng, C. Huang, Y. Li, Z. Chen, H. Wu, J. Shi, Y. Luo, D. Li, Q. Meng, Temperature-reliable low-dimensional perovskites passivated black-phase CsPbI₃ toward stable and efficient photovoltaics. *Angew. Chem. Int. Ed.* **61**, e202201300 (2022).

50. J. Wang, J. Zhang, Y. Zhou, H. Liu, Q. Xue, X. Li, C.-C. Chueh, H.-L. Yip, Z. Zhu, A. K. Y. Jen, Highly efficient all-inorganic perovskite solar cells with suppressed non-radiative recombination by a lewis base. *Nat. Commun.* **11**, 177 (2020).

51. F. Meng, B. Yu, Q. Zhang, Y. Cui, S. Tan, J. Shi, L. Gu, D. Li, Q. Meng, C. Nan, Ge Incorporation to stabilize efficient inorganic CsPbI₃ perovskite solar cells. *Adv. Energy Mater.* **12**, 2103690 (2022).

52. CrysAlisPro (Oxford Diffraction/Agilent Technologies UK Ltd, 2020).

53. G. M. Sheldrick, SHELXT–Integrated space-group and crystal-structure determination. *Acta Crystallogr. Sect. A: Found. Adv.* **71**, 3–8 (2015).

54. O. V. Dolomanov, L. J. Bourhis, R. J. Gildea, J. A. Howard, H. Puschmann, OLEX2: A complete structure solution, refinement and analysis program. *J. Appl. Cryst.* **42**, 339–341 (2009).

55. G. M. Sheldrick, Crystal structure refinement with SHELXL. *Acta Crystallogr. Sect. C: Struct. Chem.* **71**, 3–8 (2015).

56. J. P. Perdew, K. Burke, M. Ernzerhof, Generalized gradient approximation made simple. *Phys. Rev. Lett.* **77**, 3865–3868 (1996).

57. T. D. Kühne, M. Iannuzzi, M. D. Ben, V. V. Rybkin, P. Seewald, F. Stein, T. Laino, R. Z. Khaliullin, O. Schütt, F. Schiffmann, D. Golze, J. Wilhelm, S. Chulkov, M. H. Bani-Hashemian, V. Weber, U. Borštnik, M. Taillefumier, A. S. Jakobovits, A. Lazzaro, H. Pabst, T. Müller, R. Schade, M. Guidon, S. Andermatt, N. Holmberg, G. K. Schenter, A. Hehn, A. Bussy, F. Belleflamme, G. Tabacchi, A. Glöß, M. Lass, I. Bethune, C. J. Mundy, C. Plessl, M. Watkins, J. VandeVondele, M. Krack, J. Hutter, CP2K: An electronic structure and molecular dynamics software package - Quickstep: Efficient and accurate electronic structure calculations. *J. Chem. Phys.* **152**, 194103 (2020).

58. J. VandeVondele, J. Hutter, Gaussian basis sets for accurate calculations on molecular systems in gas and condensed phases. *J. Chem. Phys.* **127**, 114105 (2007).

59. S. Goedecker, M. Teter, J. Hutter, Separable dual-space gaussian pseudopotentials. *Phys. Rev. B* **54**, 1703–1710 (1996).

60. K. Momma, F. Izumi, *VESTA 3* for three-dimensional visualization of crystal, volumetric and morphology data. *J. Appl. Cryst.* **44**, 1272–1276 (2011).

61. J. H. Heo, D. H. Kim, J. K. Park, Y. K. Choi, D. S. Lee, S. H. Im, Thermally stable inorganic CsPbI₂Br mesoscopic metal halide perovskite solar submodules. *ACS Appl. Mater. Interfaces* **11**, 43066–43074 (2019).

62. C. Liu, Y. Yang, C. Zhang, S. Wu, L. Wei, F. Guo, G. M. Arumugam, J. Hu, X. Liu, J. Lin, R. E. I. Schropp, Y. Mai, Tailoring C₆₀ for efficient inorganic CsPbI₂Br perovskite solar cells and modules. *Adv. Mater.* **32**, 1907361 (2020).

Science Advances

Retarding solid-state reactions enable efficient and stable all-inorganic perovskite solar cells and modules

Cheng Liu, Xiuhong Sun, Yi Yang, Olga A. Syzgantseva, Maria A. Syzgantseva, Bin Ding, Naoyuki Shibayama, Hiroyuki Kanda, Farzaneh Fadaei Tirani, Rosario Scopelliti, Shunlin Zhang, Keith G. Brooks, Songyuan Dai, Guanglei Cui, Michael D. Irwin, Zhipeng Shao, Yong Ding, Zhaofu Fei, Paul J. Dyson, and Mohammad Khaja Nazeeruddin

View the article online
https://www.science.org/doi/10.1126/sciadv.adg0087
Permissions
https://www.science.org/help/reprints-and-permissions

Downloaded from https://www.science.org at EPF Lausanne on August 02, 2023

Use of this article is subject to the Terms of service

Science Advances (ISSN) is published by the American Association for the Advancement of Science. 1200 New York Avenue NW, Washington, DC 20005. The title *Science Advances* is a registered trademark of AAAS.

Copyright © 2023 The Authors, some rights reserved; exclusive licensee American Association for the Advancement of Science. No claim to original U.S. Government Works. Distributed under a Creative Commons Attribution NonCommercial License 4.0 (CC BY-NC).